



# Machine learning-aided design and prediction of cementitious composites containing graphite and slag powder

Junbo Sun<sup>a</sup>, Yongzhi Ma<sup>b</sup>, Jianxin Li<sup>b</sup>, Junfei Zhang<sup>c,\*</sup>, Zhenhua Ren<sup>d</sup>, Xiangyu Wang<sup>e,f,\*\*</sup>

<sup>a</sup> School of Design and the Built Environment, Curtin University, Perth, WA, 6102, Australia

<sup>b</sup> School of Information Technology, Deakin University, Geelong, Australia

<sup>c</sup> School of Civil and Transportation Engineering, Hebei University of Technology, 5340 Xiping Road, Beichen District, Tianjin, 300401, China

<sup>d</sup> School of Building Engineering, Hunan Institute of Engineering, Hunan, 411228, China

<sup>e</sup> School of Civil Engineering and Architecture, East China Jiao Tong University, Nanchang, 330013, China

<sup>f</sup> Australasian Joint Research Centre for Building Information Modelling, Curtin University, Perth, WA, 6102, Australia

## ARTICLE INFO

### Keywords:

Random forest  
Beetle antennae search  
Machine learning  
Graphite  
Waste slag  
Compressive strength  
Electrical resistivity

## ABSTRACT

The electrically conductive cementitious composite (ECCC) offers plenty of advantages such as high conductivity and strain sensitivity. The ECCC can also act as a conductive sensor in a cathodic protection system for structural health monitoring. Before the ECCC application, it is essential to understand and predict the uniaxial compressive stress (UCS) and electrical resistivity. In this study, we produced ECCC with three conductive fillers: graphite powder (GP), waste steel slag (SS) as well as ground granulated blast-furnace slag (GGBS). By changing the content levels of the three conductive fillers, cement and curing ages, we prepared 81 mixture proportions for UCS test and 108 mixture proportions for resistivity test. The results show that although GP improves the conductivity more significantly than the other conductive fillers but it simultaneously has a higher negative influence on UCS. Meanwhile, slag solids (GGBS and SS) enhance the conductive performance but reduce UCS after their replacement ratio is larger than 20%. Compared with GGBS, ECCC containing SS has higher UCS and conductivity. Besides, we proposed a random forest (RF) based machine learning model to predict the UCS and resistivity. The hyperparameters of the RF model were tuned by the beetle antennae search (BAS) algorithm. This hybrid BAS-RF model has high prediction accuracy, as indicated by high correlation coefficients on test sets (0.986 for UCS and 0.98 for resistivity, respectively). We simulated the influence of different conductive fillers on UCS and conductivity using the developed BAS-RF model. The simulation results agree well with the results obtained by laboratory experiments. This study offers a new idea to use waste slags to produce ECCC and paves the way to intelligent construction.

## 1. Introduction

Cementitious composites are a type of popular materials in the building and construction industry due to their excellent properties such as low cost, easy application, long durability and good mechanical properties [1,2]. In addition, by introducing waste materials into the cementitious composites, the environmental problems can be mitigated [3–5]. However, as a quasi-brittle material, cracking elongation issues in these materials significantly degrade their mechanical performance [6–8]. Thereby, the electrically conductive cementitious composite (ECCC) was proposed as a feasible solution [9,10]. ECCC exhibits outstanding conductivity and can serve as a monitoring sensor to

measure internal electrical resistivity, thus providing instant information about structural changes of the structure [11–13]. A variety of conductive fillers have been introduced into ECCC to improve its electrical performance [14,15], among which the graphite powder (GP) is a promising material due to its high conductive and light-weight properties. However, in the microstructure, GP has a smooth surface that reduces the surface bonding resistance, hence degrading mechanical performance [16–19]. As a result, how to strike a balance between mechanical and conductive properties is crucial. To this end, the metal waste slags including steel slag (SS) and granulated blast-furnace slag (GGBS) from steelmaking procedure can be introduced. Both SS and GGBS have crystal and rough microstructures which can effectively

\* Corresponding author.

\*\* Corresponding author. School of Civil Engineering and Architecture, East China Jiao Tong University, Nanchang, 330013, China.

E-mail addresses: [junfei.zhang@research.uwa.edu.au](mailto:junfei.zhang@research.uwa.edu.au) (J. Zhang), [Xiangyu.wang@curtin.edu.au](mailto:Xiangyu.wang@curtin.edu.au) (X. Wang).

bond aggregates and enhance the mechanical strength and durability of cementitious composites [20–22]. Moreover, SS can serve as micro-platforms with massive square sharp edges around the surface to capture the GP, forming a conductive network [23]. As a result, the combination of the waste slags guarantees satisfying mechanical strength, desirable workability and conductive performance. Comprehensive utilization of SS, GGBS and GP in concrete can achieve cost-effective and environmentally-friendly potential and strike a balance of mechanical performance and multiple functions [24].

As a functional material, the electrical resistivity and uniaxial compressive strength (UCS) are two critical parameters for ECCC application. To estimate these parameters, samples need to be prepared in the laboratory to understand the influence of mixture proportions on UCS and resistivity. This laboratory-based method is lengthy and costly because of equipment preconfiguring and a large number of samples to prepare [25]. To apply the materials at any mixture proportion, the relationship between UCS/resistivity and influencing variables need to be built. To this end, statistical regression methods including logistic regression (LR) and multiple linear regression (MLR) have been applied. However, it is still challenging to achieve accurate prediction accuracy using such simple models due to highly non-linear relationships between UCS/resistivity and their influencing variables [26–28]. As a result, more accurate and generalized models are in great demand to assist in the construction.

In recent years, machine learning (ML) models have exhibited great potential for anticipating parameters of cementitious materials [29,30]. Among many ML models, Support Vector Regression (SVR) and Artificial Neural Network (ANN) has been extensively used to predict concrete properties, such as UCS, elastic modulus, etc. However, ANN and SVM are standalone models. Studies in other fields have proved that prediction accuracy can be significantly improved by using ensemble learning models that integrate the results of standalone models to achieve the final result [31]. Fewer studies that use ensemble learning to predict concrete parameters have been conducted in this field. Random forest (RF) is a representative ensemble learning model, which can enhance the predicting accuracy through combining the prediction results obtained by multiple regression trees and obtaining the final result by voting [32]. In comparison with ANN, RF is less likely to overfit in the small and imbalanced dataset. Compared with SVM, RF has a higher tolerance for outliers and noise in the dataset [33].

This study first systematically investigates the influence of GP, SS and GGBS on UCS and resistivity of ECCC by laboratory experiments. Then, we proposed a hybrid BAS-RF model (hyperparameters of RF are tuned by BAS) with high generalization ability for predicting UCS and resistivity of ECCC, offering a new idea to design ECCC mixture optimization. Third, the importance of input variables to conductivity and UCS of ECCC was measured by using the developed BAS-RF model.

## 2. Experimental program

### 2.1. Mixture design

The ordinary Portland cement (OPC, P.O 52.5R) was used as the main binder material with a fixed water-to-binder (OPC, GGBS and SS) ratio of 0.35. Its chemical composition and physical properties are tabulated in Table 1. Fine silica sand with size ranging between 0.2 mm and 0.4 mm and fineness modulus of 2.6 was applied as the fine aggregate. The coarse aggregate was gravel with size ranging from 5 to 10 mm. A polycarboxylate-based superplasticizer (SP, Q8081PCA, Sika Ltd, China) was incorporated in a 0.3% weight of binder material for lowering the cement sensitivity and yielding segregation intensity [34, 35].

As for the conductive fillers, GP manufactured by GRF Ltd, China was selected to be the main conductive ingredient due to its remarkable electrical resistivity (Table 2). The GP powder possesses a high purity of carbon (98.5%) with outstanding conductive performance. Also, GP has

**Table 1**

Physical properties and chemical composition of OPC.

Physical properties	OPC
Specific gravity	3.0–3.2 t/m <sup>3</sup>
Normal consistency	27%
Loss on ignition	3.80%
Fineness index	390 m <sup>2</sup> /kg
Setting time initial	120 min
Setting time final	210 min
<i>Chemical composition</i>	
CaO	63.40%
SiO <sub>2</sub>	20.10%
Al <sub>2</sub> O <sub>3</sub>	4.60%
Fe <sub>2</sub> O <sub>3</sub>	2.80%
SO <sub>3</sub>	2.70%
MgO	1.30%
Na <sub>2</sub> O	0.60%
Total chloride	0.02%

**Table 2**

Physical properties and chemical composition of GP.

Physical properties	GP
Moisture Content	0.35%
Particle size distribution	23–37.4 μm
Bulk Density	0.33 t/m <sup>3</sup>
Melting Point	4200 °C
<i>Chemical composition (%)</i>	
Carbon	98.50%
Ash Content	0.90%

smooth microstructural surface which fulfils the micro cavities among calcium silicate hydrate (C-S-H) interfaces. SS and GGBS purchased from Yuanheng Ltd, Henan Province, China was employed as another two conductive fillers. Their chemical composition and physical properties are shown in Table 3 and Table 4, respectively.

Three levels of GP-to-binder (g/b) ratios by mass were applied: 2%, 4% and 6%. Cement was replaced by the two slags (SS and GGBS) by mass. The levels of slag-to-binder (s/b) ratios were 20%, 30% and 40%. Within each s/b level, three sublevels of SS-to-GGBS (s/g) ratios by mass (25%, 50% and 75%) were also explored. For each mixture, we tested its UCS on 7, 14 and 28 days, respectively, and its resistivity on 7, 14, 21 and 28 days, respectively. A mixture batch containing three samples were tested to obtain the mean UCS/resistivity results. Finally, 81 UCS values and 108 resistivity values were collected for analysis. The specific mixture design (unit of kg/m<sup>3</sup>) is shown in Table 5 and mechanical behaviour and conductivity results are given in Appendix A.

### 2.2. Sample preparation

Dry ingredients including gravel, sand and cement were firstly mixed

**Table 3**

Physical properties and chemical composition of GGBS.

Physical properties	GGBS
Specific gravity	2.84 t/m <sup>3</sup>
Relative strength	100%
Ignition loss	0.60%
Specific surface area	472 m <sup>2</sup> /kg
Particle size distribution	23–37.4 μm
Pozzolanic Activity at 7 days	78%
<i>Chemical composition (%)</i>	
CaO	37.14%
SiO <sub>2</sub>	31.00%
Al <sub>2</sub> O <sub>3</sub>	15.60%
MgO	8.51%
SO <sub>3</sub>	2.40%
Fe <sub>2</sub> O <sub>3</sub>	1.80%
MnO	0.10%

**Table 4**  
Physical properties and chemical composition of SS.

Physical properties	SS
Temperature rise	18.8 OC
Particle size distribution	50–75 $\mu\text{m}$
Specific gravity	3.67 t/m <sup>3</sup>
Relative strength	100%
<i>Chemical composition (%)</i>	
CaO	31.49%
SiO <sub>2</sub>	14.60%
Al <sub>2</sub> O <sub>3</sub>	5.71%
MgO	13.80%
SO <sub>3</sub>	2.40%
Fe <sub>2</sub> O <sub>3</sub>	21.30%

**Table 5**  
Mix proportion of ECCC composites(kg/m<sup>3</sup>).

ID	OPC	Gravel	Sand	GP	SS	GGBS	SP
1	360	1302	884.6	9	22.5	67.5	1.35
2	360	1302	884.6	18	22.5	67.5	1.35
3	360	1302	884.6	27	22.5	67.5	1.35
4	360	1302	884.6	9	45	45	1.35
5	360	1302	884.6	18	45	45	1.35
6	360	1302	884.6	27	45	45	1.35
7	360	1302	884.6	9	67.5	22.5	1.35
8	360	1302	884.6	18	67.5	22.5	1.35
9	360	1302	884.6	27	67.5	22.5	1.35
10	315	1302	884.6	9	45	90	1.35
11	315	1302	884.6	18	45	90	1.35
12	315	1302	884.6	27	45	90	1.35
13	315	1302	884.6	9	67.5	67.5	1.35
14	315	1302	884.6	18	67.5	67.5	1.35
15	315	1302	884.6	27	67.5	67.5	1.35
16	315	1302	884.6	9	90	45	1.35
17	315	1302	884.6	18	90	45	1.35
18	315	1302	884.6	27	90	45	1.35
19	270	1302	884.6	9	67.5	112.5	1.35
20	270	1302	884.6	18	67.5	112.5	1.35
21	270	1302	884.6	27	67.5	112.5	1.35
22	270	1302	884.6	9	90	90	1.35
23	270	1302	884.6	18	90	90	1.35
24	270	1302	884.6	27	90	90	1.35
25	270	1302	884.6	9	112.5	67.5	1.35
26	270	1302	884.6	18	112.5	67.5	1.35
27	270	1302	884.6	27	112.5	67.5	1.35

for 5 min in a container. The GGBS and SS were then dispersed into the holder for another 30-s mixing to guarantee an even distribution state. In the meantime, a solution containing SP and water was prepared and divided into two halves. The first half was added to the dry composites and mixed for 80 s. After that, the other half solution was sprinkled into the composite with an extra 200-s mixing. After 30-s vibration to diminish caught bubbles, the composite was finally cast in steel moulds with a size of 400 mm × 100 mm × 100 mm for resistivity test and 50 × 50 × 50 mm for UCS test, respectively. All samples were stored in the moist cabinet to fulfil the required curing period with humidity at 95 ± 5% and a curing temperature at 20 ± 1 °C.

### 2.3. Electrical test

The electrical resistivity of the concrete was tested by using a four-probe measurement method on 7, 14, 21, and 28 days, respectively (see Fig. 1). Four brass wire mesh with pore size of 0.3 mm was used as electrodes. The electrodes were cut into 100 mm × 100 mm and were embedded into the sample (400 mm × 100 mm × 100 mm) with equal spacing of 120 mm. For each batch, three resistivity values were recorded by the digital multimeter (Keithley Model 2002) via copper wire, and their mean value was taken. If the deviation between mean value and each resistivity is less than 15%, the final resistivity is

determined as mean value. Otherwise, the resistivity has to be measured again until the value fits the deviation requirement. Therefore, 324 samples in total were tested. The resistivity ( $\rho$ ) is calculated as:

$$\rho = \frac{UA}{IL} \quad (1)$$

where  $U$  is the voltage;  $A$  is the cross-sectional area of the sample;  $I$  is the electric current and  $L$  is the distance between electrodes.

### 2.4. Mechanical test

In this study, the UCS was measured as per GB/T 50081-2002 [36] on 7, 14, and 28 days, respectively. A servo-hydraulic machine with a continuous loading rate of 0.5 MPa/s was applied to obtain the stress-strain curves of the samples [37]. The deformation and stress distribution was measured by its electronic system with an max 1% accuracy.

## 3. Machine learning methods

### 3.1. RF algorithm

By combining the bootstrap and aggregation strategies, the RF algorithm has been widely used for regression and classification tasks [38]. The RF model uses the bagging method to combine all the regression trees (RTs). Bagging is one of the approaches of model averaging and can reduce variance and avoid overfitting issues. Fig. 2 illustrates the detailed training procedure of the RF model. In this figure,  $T_n^b$  is a bootstrap sample that has  $n$  samples randomly selected from the training set  $T$  at a selective probability ( $1/n$ ). The symbol  $\theta$  represents an independently distributed vector.  $\hat{a}$  is a regression tree,  $x$  is the input variable and  $y$  is the output variable. We train  $b$  RTs:  $\hat{a}(x, T_n^{\theta_1})$ ,  $\hat{a}(x, T_n^{\theta_2})$ , ...,  $\hat{a}(x, T_n^{\theta_b})$  on  $b$  bootstrap samples  $\{T_n^{\theta_1}, T_n^{\theta_2}, \dots, T_n^{\theta_b}\}$  and then average the results of these  $b$  outputs to obtain the final result of RF.

### 3.2. Baseline models

In this study, the BAS-RF prediction results are compared with two fundamental models: LR and MLR. The LR model with multiple predictor variables can be expressed as follows [39].

$$\ln \frac{p}{1-p} = b_0 + \sum_{k=1}^n b_k x_k \quad (2)$$

where  $p$  represents a probability variable;  $x_k$  are the independent variables (input variables) with its coefficient being  $b_k$  in the dataset;  $b_0$  denotes the constant coefficients of the LR model; The MLR model is given by Ref. [40].

$$Y = \beta_0 + \beta_1 x_1 + \beta_2 x_2 + \dots + \beta_n x_n \quad (3)$$

where  $Y$  is the output variable in the dataset;  $x$  is the input variable in the dataset, and  $\beta$  is the coefficient of the MLR model.

### 3.3. BAS algorithm

In this study, the hyperparameters of RF are tuned by BAS algorithm which demonstrates outstanding performance in solving optimization problems and becomes very popular recently. This algorithm derives from longhorn beetles nature behaviour (Fig. 3) [41].

In this algorithm, a random direction vector ( $\mathbf{b}$ ) is firstly defined as follows

$$\mathbf{b} = \frac{\text{rnd}(k, 1)}{\text{rnd}(k, 1)} \quad (4)$$

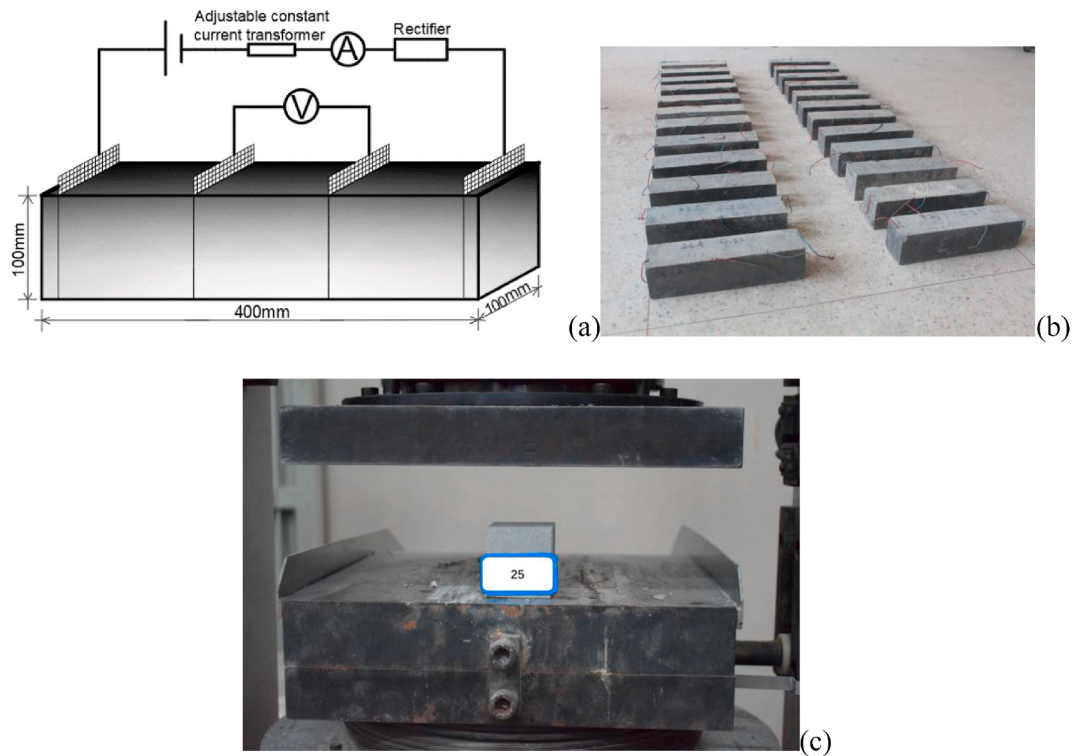


**Fig. 1.** (a) Four-probe method diagram (b) conductive experiment sample,(c) compressive experiment set-up.

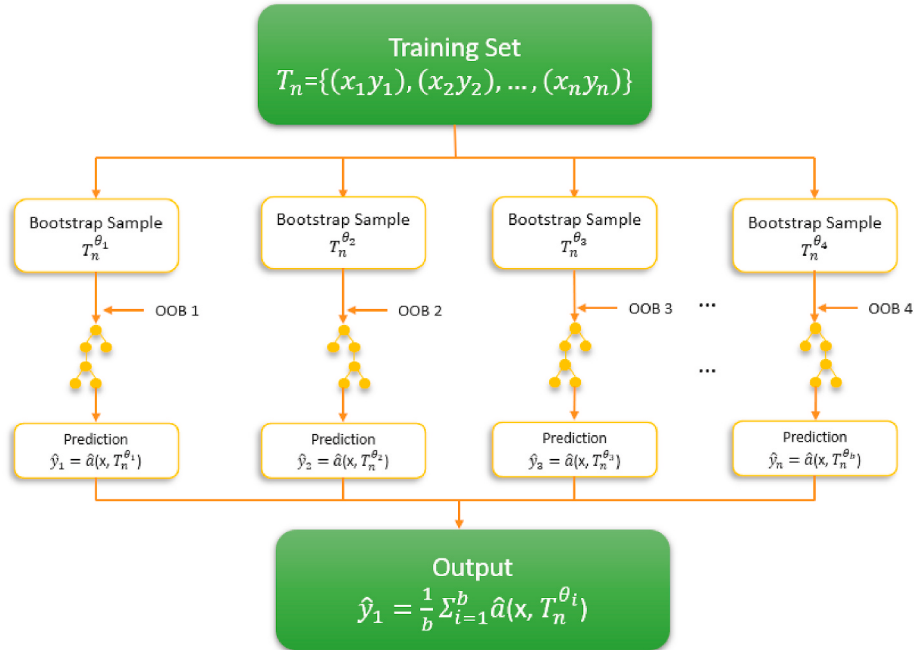


**Fig. 2.** Construction of an RF model.

where rand ( $k,1$ ) is random function with  $k$  dimensions, the left-hand side ( $\mathbf{x}_l$ ) and right-hand side ( $\mathbf{x}_r$ ) can be given by

$$\mathbf{x}_l = \mathbf{x}^t + d^t \mathbf{b} \quad \mathbf{x}_r = \mathbf{x}^t - d^t \mathbf{b} \quad (5)$$

where  $d^t$  is the antennae length at time  $t$ . The fitness is determined as a function of position  $\mathbf{x}$ , and the searching performance is thereby written as

$$\mathbf{x}^t = \mathbf{x}^{t-1} + \delta^t \mathbf{b} sign(f(\mathbf{x}_r) - f(\mathbf{x}_l)) \quad (6)$$

where  $\delta^t$  is the beetle step size; and  $f(\mathbf{x})$  is the fitness function. The step size and antennae length is thereby updated as

$$d^t = 0.95d^{t-1} + 0.01 \quad (7)$$

$$\delta^t = 0.95\delta^{t-1} \quad (8)$$

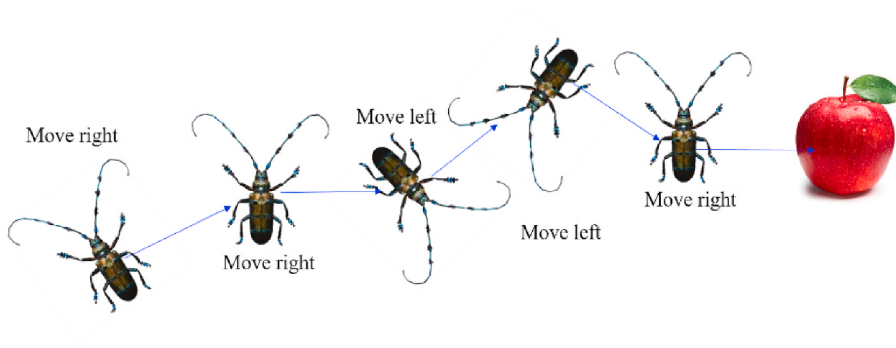


**Fig. 3.** Searching behaviour of the beetle.

### 3.4. Performance evaluation measure

The correlation coefficient (R) and root means square error (RMSE) is used to evaluate the prediction results of the ML models. RMSE and R are defined as

$$\text{RMSE} = \sqrt{\frac{1}{N} \sum_{i=1}^N (y_i^* - y_i)^2} \quad (9)$$

$$R = \frac{\sum_{i=1}^N (y_i^* - \bar{y}^*)(y_i - \bar{y})}{\sqrt{\sum_{i=1}^N (y_i^* - \bar{y}^*)^2} \sqrt{\sum_{i=1}^N (y_i - \bar{y})^2}} \quad (10)$$

where  $N$  means the dataset sample number;  $y_i^*$  is the predicted output by the ML models;  $y_i$  is the actual output in the dataset;  $\bar{y}^*$  is predict mean value, and  $\bar{y}$  is the observed mean value in the dataset.

### 3.5. Hyperparameter tuning

In the training process of RF, two hyperparameters need to be optimized: minimum sample number of a leaf node (`minNumLeaf`) and the total number of trees (`numTree`) [42]. The `minNumLeaf` value determines the correlation among regression trees, while the `numTree` value influences RF's operating efficiency and generalization ability. Traditionally, these hyperparameters are determined by artificial selection which is not efficient and cannot ensure the obtained hyperparameters are optimal. Optimization algorithm is an alternative method that can automatically find optimal hyperparameters of RF with high efficiency. Metaheuristic optimization algorithms based on swarm intelligence (SI) have been widely used to tune hyperparameters of ML models [43]. These algorithms include Particle Swarm Optimization (PSO), Genetic Algorithm (GA) and Firefly Algorithm (FA). These SI-based optimization algorithms use a swarm of particles to search for the global optimum, which is computationally intensive. To reduce computational resource, Beetle Antennae Search (BAS) was developed recently [44]. It uses one particle to search and thus the time and space complexity is considerably reduced. Therefore, in this study, we will develop a BAS-RF model (hyperparameters of RF are tuned by BAS) to predict UCS and resistivity of ECCC.

During model training, to avoid overfitting problems caused by small datasets,  $k$ -fold cross-validation (CV) is usually used in training ML models. The  $k$ -fold CV, also known as rotation estimation is a resampling method used to assess ML models within a range of data samples (Fig. 4). The  $k$  is a single parameter which means that a given data sample is split into  $k$  groups and  $k$  is given by 10 in this research according to the previous study, [45]. In detail, the training set size is devided into 10 folds, and 9 folds are used to train the RF model by BAS algorithm and the remaining one is used for validation. RMSE will be calculated on this validation set. Thus, the optimal hyperparameters are picked out after convergence has been reached. This procedure runs for 10 times in each

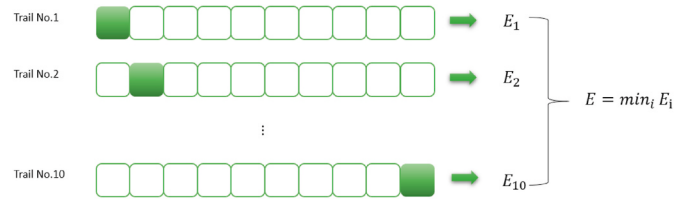


**Fig. 4.** 10-fold CV.

fold with an alternative set like validation set. The 10 results are then averaged to obtain the final hyperparameters that will be used in this research. The RF model with best hyperparameters will be verified by 30% data samples to check whether the overfitting issue occurs. The procedure of model training using BAS and 10-fold CV is demonstrated in Fig. 5.

## 4. Experiment and simulation results and discussion

### 4.1. Laboratory tests

#### 4.1.1. Result of mechanical test

Fig. 6a denotes the influence of GP and slag solids (GGBS and SS) on UCS with the ratio of SS to GGBS being 1:1. It can be seen that in comparison with the control sample with a UCS of 50 MPa, the UCS of the sample with 2% g/b and 20% s/b ratio increases by 1.6%. However, when s/b ratio continues to increase to 40%, the UCS witnesses a 25.6% decrease. The possible reason for the increase of UCS is that at a lower GP ratio (2%) and s/b ratio (20%), the crystal structure of waste slags that reinforces the interface transition zone (ITZ) and improves microstructural friction [46–48]. However, excessive slags may break the uniform particle size distribution and the increased aggregate gaps cannot be filled with an insufficient cement binder [49–52]. Thereby, the bonding fraction in micro-structural magnitudes is reduced and mechanical strength also decreases [53]. It can be also observed that for higher g/b ratios, the UCS dramatically decreases with increasing the g/b ratio during the entire hydration period. This is attributed to its relatively smooth surface and reduces the bonding effect of aggregate ITZ [54–56]. When s/b ratio is 40% and g/b ratio increases to 6% from 2%, the UCS shows a 25.6%–45.6% decrease at 28 days, compared with the control sample. Thereby, even with the improving effect of slag solids, a 4% threshold of g/b fraction is concluded in order to ensure sufficient UCS performance.

Fig. 6b demonstrates the influence of GGBS and SS upon UCS with a fixed g/b ratio of 4%. From the previous analysis, when the s/b ratio exceeds 20%, UCS decreases with increasing s/b ratio. However, the extent of influence is different. Compared to GGBS, SS demonstrates a minor effect on UCS during the hydration procedure. For instance, for a 30% s/b ratio, the ECCC containing 10% SS and 20% GGBS has a UCS of 33.8 MPa at 28 days, which is lower than that with 15% SS and 25%

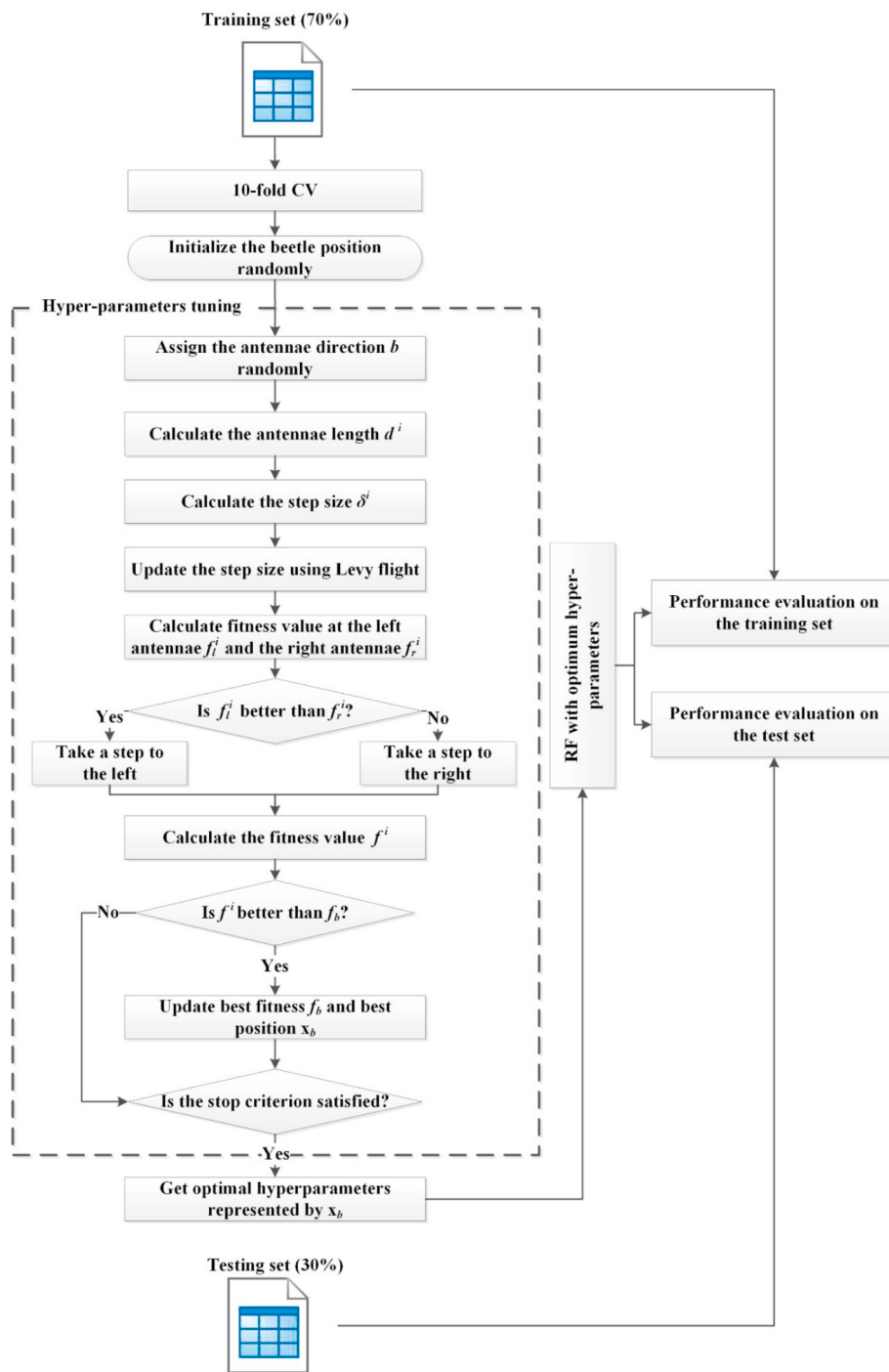


Fig. 5. Model training using BAS and 10-fold CV.

GGBS ( $UCS = 35.9$  MPa), and lower than that with 20% SS and 10% GGBS ( $UCS = 40$  MPa). The possible reason is that SS has massive square crystals with sharp edges around 500 nm to 1  $\mu\text{m}$  on the surface. The unique structure significantly enhances the bonding strength of the ITZ that improves toughness development and mechanical behaviour [57–59]. Moreover, the concrete curing time also has a great influence on UCS. Overall, ECCC gains 65% of its final 28-day UCS after 7 days of curing, and 90% after 14 days.

#### 4.1.2. Result of electrical test

Fig. 7a shows the influences of GP, GGBS and SS on ECCC conductive performance with SS-to-GGBS ratio being 1:1. It can be seen that the

resistivity of ECCC is most significantly affected by GP. For instance, the group containing 30% slag solid, when g/b fraction rises from 2% to 6%, a 97.6% decrease in the resistivity of ECCC is observed. It can be also observed that the resistivity of ECCC also decreases with increasing the s/b ratio. For the samples with a constant g/b ratio of 4% at 28 days, it can be seen that when the s/b value shifts from 20% to 40%, the resistance of ECCC decreases by 96.7% (from 151125  $\Omega \text{ cm}$  to 5050  $\Omega \text{ cm}$ ). Among all designs, a 15 wt% ratio of GGBS, 20 wt% of SS, and 4 wt% of GP are explored as the optimum design with 41.5 MPa of compressive strength, and 1054  $\Omega \text{ cm}$  of resistance. The resistivity is suitable for structural health monitoring and also supply strong loading capacity as cementitious material.

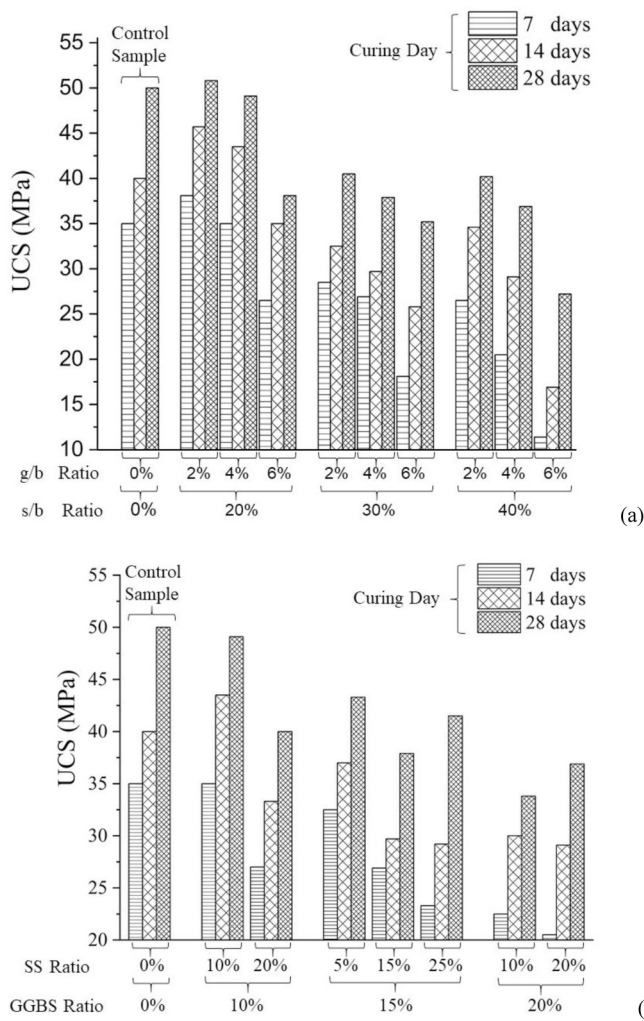


**Fig. 6.** UCS composites at different curing ages. (a) Influence of GP and slag (SS: GGBS = 1:1) on UCS and (b) Influence of SS and GGBS on UCS with a constant g/b ratio of 4%.

Fig. 7b shows how SS and GGBS affects the resistivity with a fixed g/b ratio of 4%. Both ingredients reduce the resistivity of ECC, but SS has a more significant influence. For a 20% GGBS content, if SS ratio increases from 10% to 20%, the conductivity of ECC decreases by 90.0% from  $49978 \Omega \text{ cm}$  to  $5050 \Omega \text{ cm}$  at 28 days, while for a 20% SS ratio, when GGBS increases from 10% to 20%, the conductivity of ECC decreases by 47.2% from  $9559 \Omega \text{ cm}$  to  $5050 \Omega \text{ cm}$ . Thereby, the SS effectively improves the conductivity and also compensates the UCS reduction caused by the lubrication effect of GP. As for the influence of curing time upon conductivity, the concrete at early ages tends to have a lower conductivity than fully hydrated concrete among all ECC samples. This phenomenon indicates that water molecules positively affect the resistivity development [60–62]. Moreover, the outstanding resistivity lay the foundation for self-sensing repeatable capabilities in real application of structural health monitoring. This is because the repeatable electrical resistivity can thoroughly analyze the loading damage using piezoelectric effect [63–65].

Fig. 8 shows the comparison of the relationship of UCS and resistivity with varying conductive materials. The figure clearly clarifies that the addition of GP improves conductive performance but dramatically decreases UCS. The addition of SS and GGBS overall negates mechanical strength while improves resistivity distribution. In fixed total waste slag ratio, the incorporation of SS improves both compressive and conductive property.

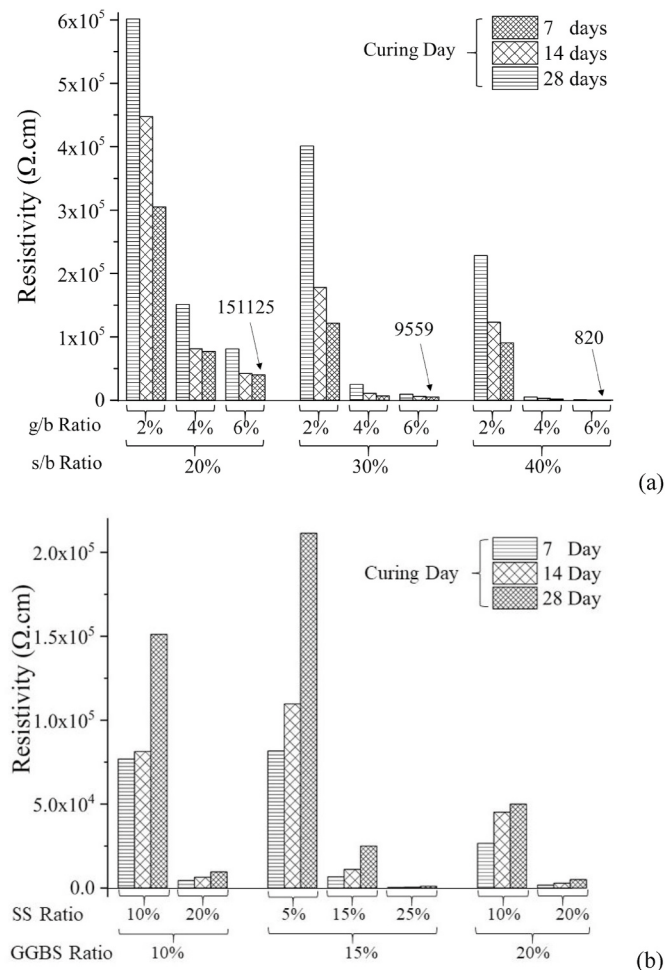


**Fig. 7.** Resistivity of ECC composites at different curing ages. (a) Influence of GP and slag (SS: GGBS = 1:1) on the resistivity of ECC and (b) Influence of SS and GGBS on the resistivity of ECC with a constant g/b ratio of 4%.

#### 4.1.3. Result of SEM

Fig. 9 shows the microstructural characteristics of ECC (Mix 12). It can be observed that GP, SS and GGBS distribute uniformly in the interfacial zone (ITZ) between aggregates and hardened C-S-H gel, ensuring a homogeneous microstructure like a conductive network to enhance the resistivity. Besides, the SS and GGBS behaves as rigid backbone and fulfills the gaps within the C-S-H structure to enhance bonding performance [66–68]. As a result, the ITZ between composite matrix and functional aggregates is reinforced and mechanical behaviour of ECC is improved.

#### 4.2. Modelling result for uniaxial compressive stress

The numerical predicted mechanical behaviour and resistivity results are given in Appendix B.

##### 4.2.1. Hyperparameter tuning for UCS prediction

In the procedure of 10-fold CV, we obtain 10 RMSE values on 10 validation sets (Fig. 10a). It can be observed that the model achieves the smallest RMSE at Fold 7. In this fold, the RMSE change during hyperparameter tuning on the training set is plotted in Fig. 10b. The best-known RMSE decreases significantly within the first several iterations and converges within 20 iterations. This result suggests BAS has higher efficiency in tuning hyperparameters of RF when modelling UCS. Finally, the final hyperparameters are obtained by averaging the 10 sets of hyperparameters: minNumLeaf = 1 and numTree = 72.

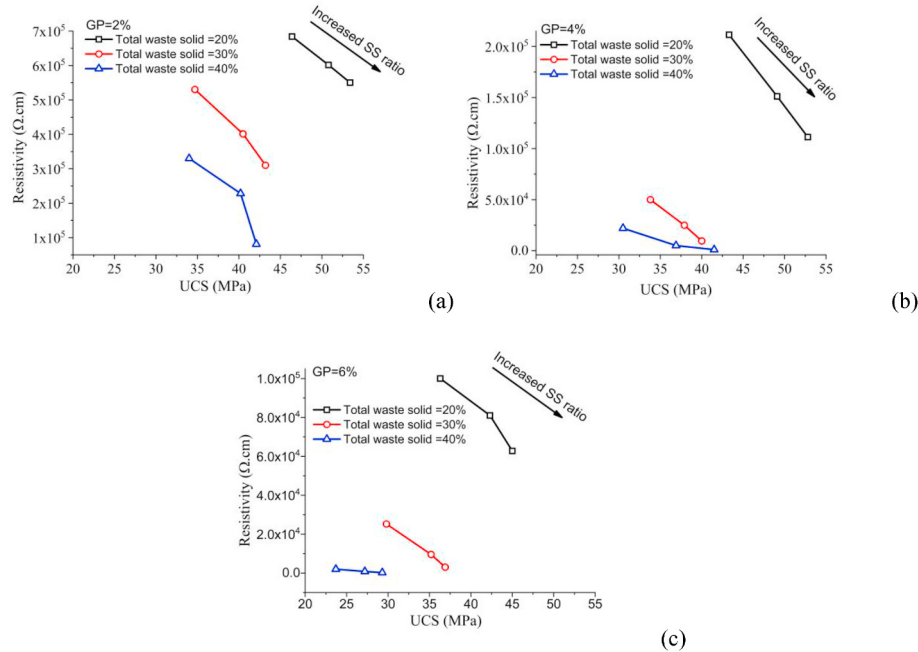


**Fig. 8.** Comparison of UCS and resistivity at different GP ratios (a) g/b ratio of 2% and (b) g/b ratio of 4% and g/b ratio of 6%.

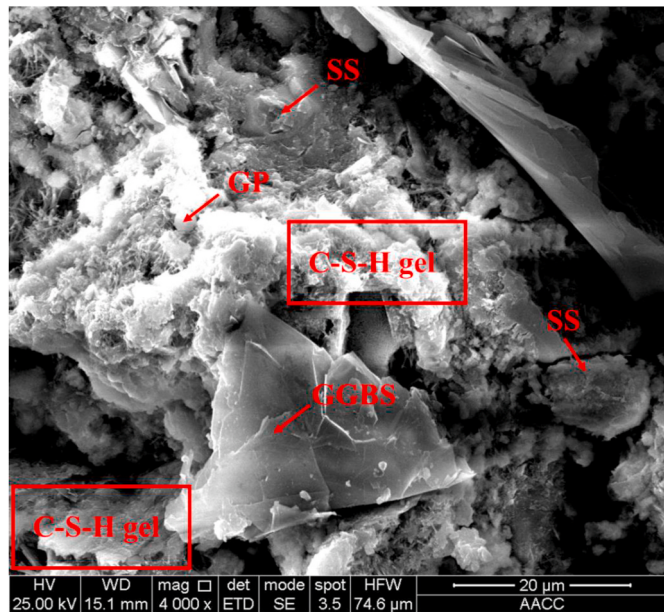


**Fig. 9.** Microscale investigation of ECCC composite at 20  $\mu\text{m}$  magnification.

#### 4.2.2. Performance of BAS-RF for UCS prediction

After obtaining optimal hyperparameters of RF, we predict UCS on the training and validation sets, respectively, as shown in Fig. 11. It can be seen that most of the prediction errors are relatively small, on the training set (Fig. 11a) and test set (Fig. 11b). The errors are also presented in a box plot in Fig. 11c. From this figure, we can see that BAS-RF model has the smallest prediction errors in comparison with the two baseline models: LR and MLR. On the test set, low RMSE (1.97 MPa), and high R-value (0.986) suggest the BAS-RF model has high prediction accuracy for predicting UCS of ECCC (see Fig. 11d). Besides, the RMSE and R values on the test set are close to those on the training set, indicating overfitting issues are not produced.

#### 4.2.3. Parametric study and variable importance for UCS prediction

To further verify the robustness of the proposed BAS-RF model for predicting UCS, we conducted a parametric study for the three conductive materials: GP, SS and GGBS. Each variable varies within the range of the dataset with other variables fixed to their mean values. It can be seen that the predicted UCS decreases with increasing GGBS (Fig. 12a), SS (Fig. 12b) or GP (Fig. 12c). This simulation result conforms to that obtained by laboratory experiments (Appendix A), implying that the BAS-RF model is robust to capture the pattern of UCS change of ECCC.

Moreover, the variables importance results are measured by obtaining the percentage decrease in prediction error on OOB samples, as shown in Fig. 12d. It is not superized that curing age is the most important variable to the development of UCS, followed by the content of OPC. It is well known that concrete gains strength rapidly within initial days after casting due to hydration of cement [69]. Of the three conductive materials, GP has the highest importance on the UCS of SCC, while SS is the least important variable. This result is consistent with the experimental result, suggesting that the BAS-RF model is accurate in explaining variable importance.

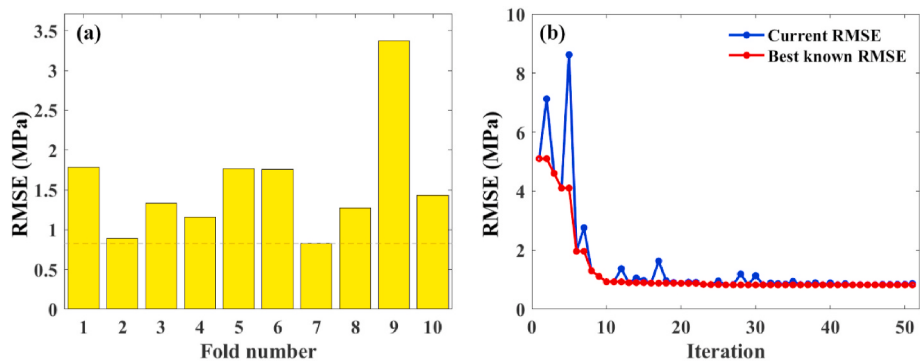
#### 4.3. Modelling result for resistivity

##### 4.3.1. Hyperparameter tuning for resistivity prediction

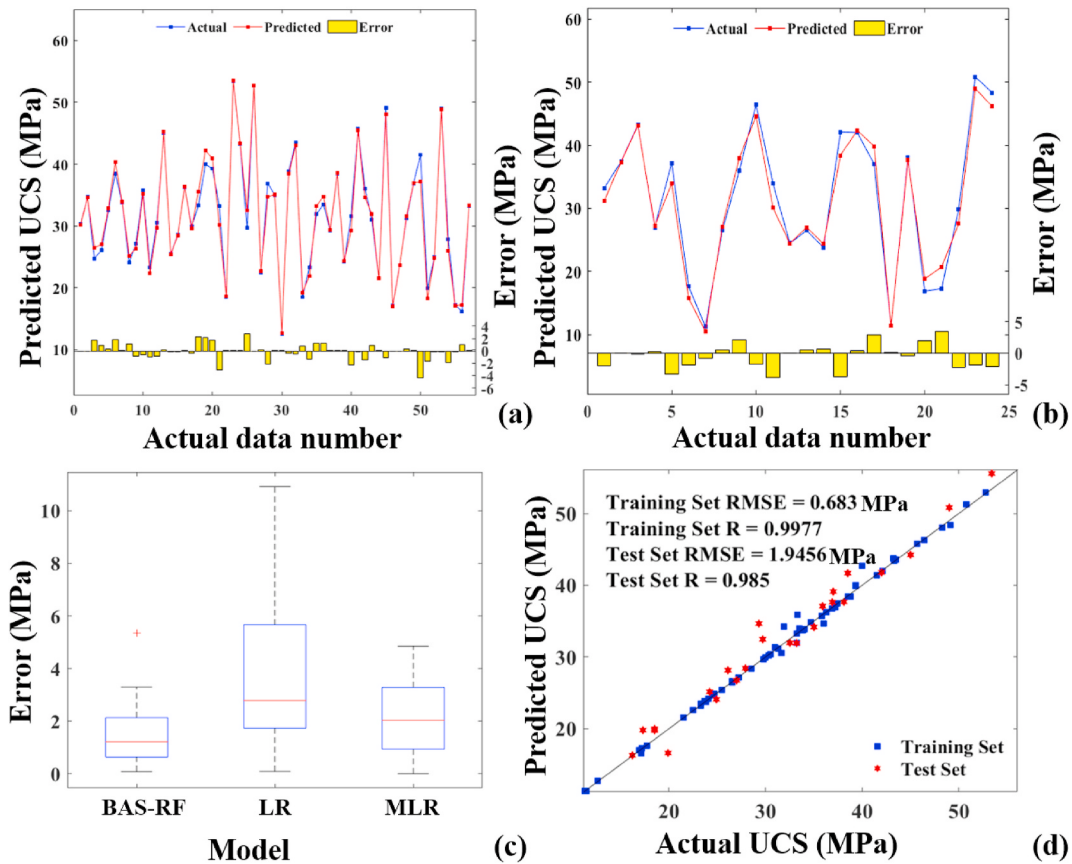
In the process of model training for predicting resistivity of ECCC, BAS is also employed to tune hyperparameters of RF. It can be observed from Fig. 13a that RMSE reaches the minimum at the fourth fold where the corresponding RMSE change with iteration is plotted in Fig. 13b. The curve converges at the tenth iteration, implying BAS can find optimal hyperparameters of RF with high efficiency. The final hyperparameter is the mean value of the 10 optimal hyperparameters obtained from the 10 folds: minNumLeaf = 1 and numTree = 84.

##### 4.3.2. Performance of BAS-RF for resistivity prediction

The BAS-RF model with optimal hyperparameters is applied to predict resistivity of ECCC on the training and test sets, respectively, as shown in Fig. 14. Although most of the errors between predicted and actual resistivity values are small on the training set (Fig. 14a) and test set (Fig. 14b), several comparatively large errors can be observed. From



**Fig. 10.** Hyperparameter tuning on the training set for uniaxial compressive stress prediction: 10 RMSE values from 10 validation sets (a) and RMSE change at the seventh iteration (b).



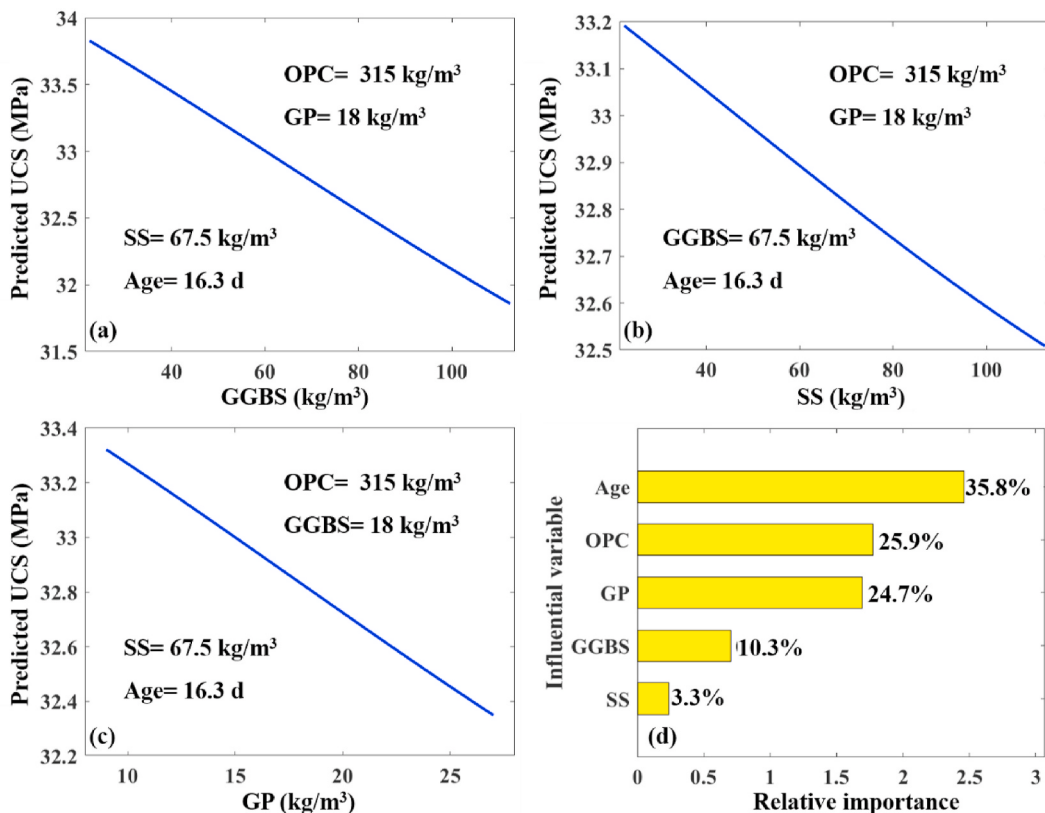
**Fig. 11.** Performance of RF-BAS model for prediction of uniaxial compressive stress: Error bars between predicted and actual values on training (a) and test (b) set, respectively; Box plot of errors between predicted and actual values on the test set (c) and scatter plot showing the relationship between actual and predicted on the dataset (d).

Fig. 14d, it can be seen that these relatively large errors correspond to relatively large resistivity values. This may be caused by insufficient training data for large resistivity values in the dataset. The performance of the RF model is compared with two baseline models on the test set: LR and MLR using a box plot, as shown in Fig. 14c. It can be seen that RF achieves smaller values for all the statistical metrics, indicating RF has the highest accuracy for predicting resistivity of ECCC. In addition, the box plot obtained by RF is the shortest, indicating overall actual data have a high level of agreement with each other.

#### 4.3.3. Parametric study and variable importance for resistivity prediction

Similar to UCS prediction, we also conduct a parametric study for the three conductive materials: GP, SS and GGBS (see Fig. 15). These

variables vary within the range of the dataset with others fixed to their mean value. It can be observed that the addition of the three materials causes a decrease in resistivity, i.e.: an increase in conductivity. This pattern agrees well with the experimental results, suggesting the BAS-RF model is accurate in modelling resistivity of ECCC. The variable importance calculated by RMSE is shown in Fig. 15d. It can be seen that GP has the most significant influence on resistivity with a relative importance of 54.1%, followed by SS with a relative importance of 18.6%. This result agrees well with the experimental result in Figure that shows GP reduces the resistivity of ECCC more significantly than other conductive materials. It is shown that GGBS has the least influence (5.8%) on the resistivity of ECCC. Therefore, GGBS is not recommended as conductive materials among the three admixtures.



**Fig. 12.** Variation of GGBS (a), SS (b) and GP (c) with other variables fixed to their mean value; and variable importance obtained by RF (d) for UCS prediction.

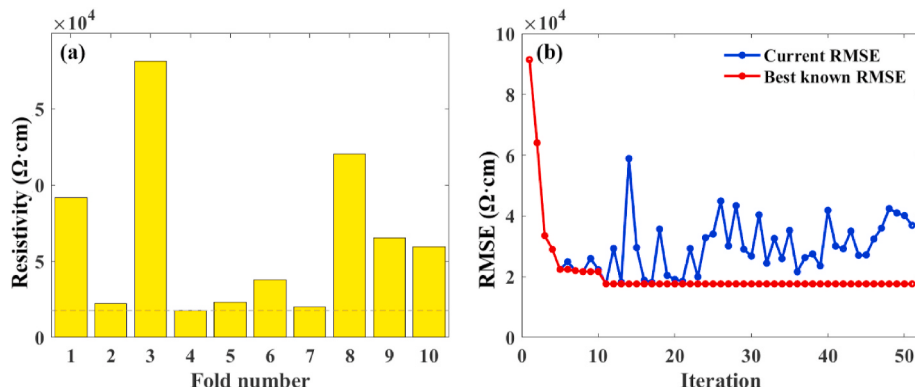


**Fig. 13.** Hyperparameter tuning on the training set for resistivity prediction: 10 RMSE values from 10 validation sets (a) and RMSE change at the seventh iteration (b).

## 5. Conclusion

In this study, the variation of contents of GP and waste slags (SS and GGBS) on UCS and electrical resistivity were explored by conducting laboratory experiments. In addition, we proposed a nature-inspired RF algorithm to model the UCS and electrical resistivity. The simulation results agree well with the experimental results. The obtained results are concluded as follows.

- 1) The UCS of ECCC significantly decreases with only a small portion of GP content due to its lubrication effect. A 4% GP ratio is recommended to achieve satisfactory mechanical and electrical properties of ECCC.
- 2) The UCS is slightly enhanced when s/b ratio is less than 20% after which, UCS decreases dramatically. However, the extent of influence

is different. Compared to GGBS, SS demonstrates a less negative impact on uniaxial compressive stress during the hydration period.sli

- 3) The conductivity is improved by the addition of GP, SS and GGBS. Of the three conductive fillers, the GP demonstrates the highest enhancement effect. Compared with GGBS, the SS is superior because it has a less negative influence on UCS and higher conductivity.
- 4) The hybrid BAS-RF model has high accuracy in predicting UCS and resistivity with correlation coefficients of 0.986 and 0.98, respectively on the 30% test sets. The results of the parametric study simulated by the RF model agree well with the experimental results.
- 5) Variable importance measured by the RF shows that age has the most significant influence on the UCS, while GP is the most important variable for resistivity. This result also confirms the experimental result.

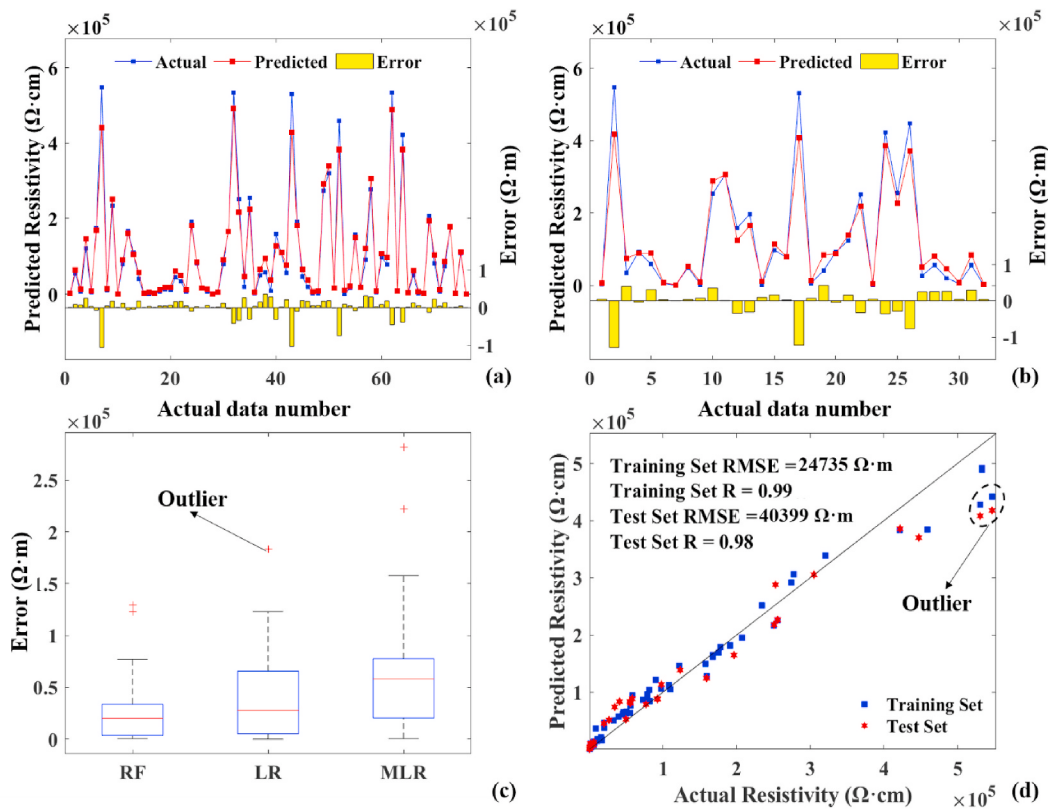


**Fig. 14.** Performance of RF-BAS model for prediction of Resistivity: Error bars between predicted and actual Resistivity values on training (a) and test (b) set, respectively; Box plot of errors between predicted and actual UCS values on the test set (c) and scatter plot showing the relationship between actual and predicted UCS on the dataset (d).

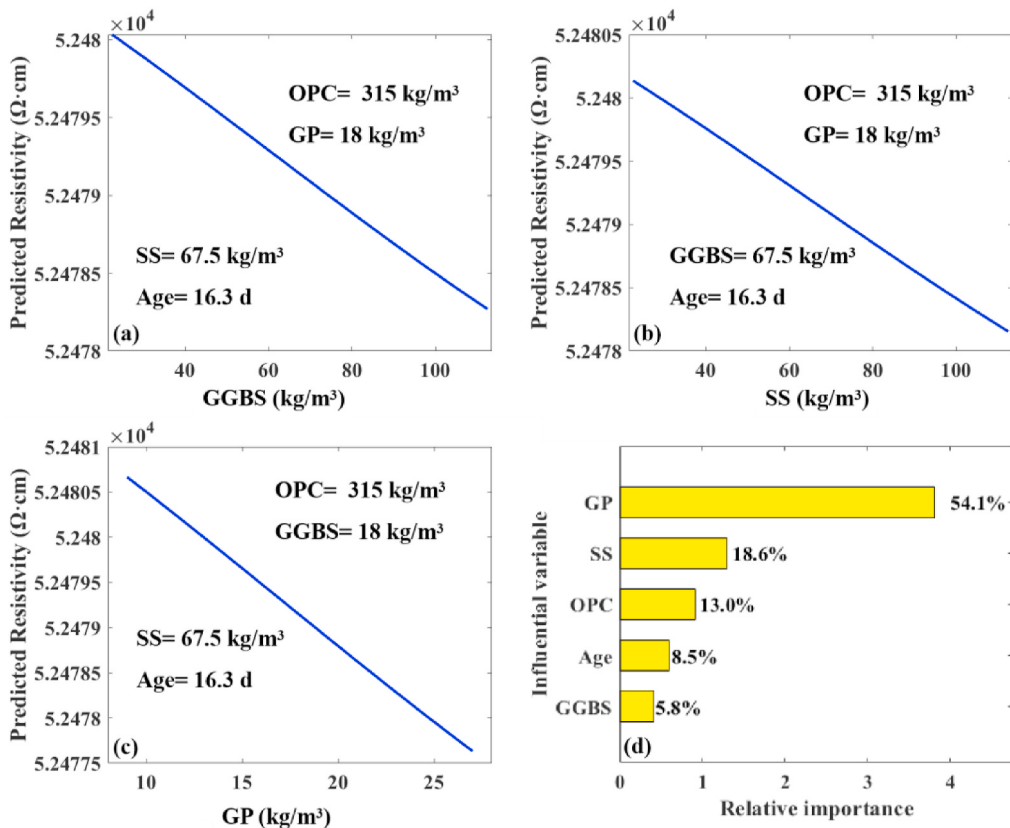


**Fig. 15.** Variation of GGBS (a), SS (b) and GP (c) with other variables fixed to their mean value; and variable importance obtained by RF (d) for resistivity prediction.

In future work, more conductive waste materials should be introduced to propose better electrical and mechanical performance. And this paper is only a primary attempt in prediction ECCC properties with a limited number of data. The work needs to be further improved by obtaining more data to train our proposed ML model. In addition, versatile influencing variables can be collected and carefully explored, including fibre materials and other waste materials. Furthermore, other advanced ML models should be introduced in their future to model properties.

## Author statement

Junbo Sun: Conceptualization, Methodology, Software, Writing – original draft preparation. Yongzhi Ma: Data curation, Supervision, Writing – review & editing. Jianxin Li: Supervision, Revising. Junfei Zhang: Supervision, Writing – review & editing. Zhenhua Ren:

## Appendix A

ID	GP	SS	GGBS	Compressive strength (Mpa)			Resistivity ( $\Omega\text{-cm}$ )			
				7d	14d	28d	7d	14d	21d	28d
1	2%	5%	15%	35.8	42	46.4	234286	274286	422010	684174
2	4%	5%	15%	32.5	37	43.3	81619	109676	107975	211377
3	6%	5%	15%	25.5	31	36.3	50239	73206	92344	999878
4	2%	10%	10%	38.1	45.7	50.8	304972	447514	533701	601659
5	4%	10%	10%	35	43.5	49.1	76807	81325	159036	151125
6	6%	10%	10%	26.5	36	39.3	40000	40941	79058	81032
7	2%	15%	5%	38.5	49	53.4	252703	320656	530888	550322
8	4%	15%	5%	37.4	48.3	52.8	54720	78731	97715	121227
9	6%	15%	5%	28.5	36.9	45	33333	54902	58169	62788
10	2%	10%	20%	24.5	31.3	34.7	277754	459144	547005	530416
11	4%	10%	20%	22.5	30	33.8	26605	45183	49541	49978
12	6%	10%	20%	17.7	23.3	29.8	8400	19700	20052	25199
13	2%	15%	15%	26.5	33.5	38.5	121673	177947	250950	401248
14	4%	15%	15%	24.9	29.7	35.9	6701	11082	15893	24985
15	6%	15%	15%	17.1	23.8	33.2	4963	5948	6277	9559
16	2%	20%	10%	30.3	38.8	43.2	157895	196382	191447	310133
17	4%	20%	10%	27	33.3	40	4482	6436	6413	9599
18	6%	20%	10%	19.9	24.7	36.9	1362	1911.2	1888	3025
19	2%	15%	25%	18.5	27.9	34	175683	207338	255611	330117
20	4%	15%	25%	17.2	24.2	30.5	10454	12924	16945	22055
21	6%	15%	25%	11.3	16.2	23.7	929	1230	1705	1995
22	2%	20%	20%	21.5	31.6	37.2	90252	123287	167528	228359
23	4%	20%	20%	18.5	26.1	31.9	1767	2912	5101	5050
24	6%	20%	20%	11.4	16.9	27.2	393	476	738	820
25	2%	25%	15%	24.1	33.2	42.1	34311	46055	55596	81055
26	4%	25%	15%	23.3	33.2	41.5	332	505	674	1054
27	6%	25%	15%	12.6	17.3	29.3	88	123	202	250

## References

- S. Chen, M. Hassanzadeh-Aghdam, R. Ansari, An analytical model for elastic modulus calculation of SiC whisker-reinforced hybrid metal matrix nanocomposite containing SiC nanoparticles, *J. Alloys Compd.* 767 (2018) 632–641, <https://doi.org/10.1016/j.jallcom.2018.07.102>.
- Z. Huang, S. Yi, H. Chen, X. He, Parameter analysis of damaged region for laminates with matrix defects, *J. Sandw. Struct. Mater.* (2019), <https://doi.org/10.1177/1099636219842290>, 1099636219842290.
- H. Yu, X. Zhu, G. Qian, X. Gong, X. Nie, Evaluation of phosphorus slag (PS) content and particle size on the performance modification effect of asphalt, *Construct. Build. Mater.* 256 (2020) 119334, <https://doi.org/10.1016/j.conbuildmat.2020.119334>.
- C. Cai, X. Gao, Q. Teng, R. Kiran, J. Liu, Q. Wei, Y. Shi, Hot isostatic pressing of a near  $\alpha$ -Ti alloy: temperature optimization, microstructural evolution and mechanical performance evaluation, *Mater. Sci. Eng., A* (2020) 140426, <https://doi.org/10.1016/j.msea.2020.140426>.
- P. Wang, T. Yao, Z. Li, W. Wei, Q. Xie, W. Duan, H. Han, A superhydrophobic/electrothermal synergistically anti-icing strategy based on graphene composite, *Compos. Sci. Technol.* 198 (2020) 108307, <https://doi.org/10.1016/j.compscitech.2020.108307>.
- Z. Wei, W. Chen, Z. Wang, N. Li, P. Zhang, M. Zhang, L. Zhao, Q. Qiang, High-temperature persistent luminescence and visual dual-emitting optical temperature sensing in self-activated CaNb<sub>2</sub>O<sub>6</sub>: Tb<sup>3+</sup> phosphor, *J. Am. Ceram. Soc.* (2020), <https://doi.org/10.1111/jace.17579>.
- C. Zhang, H. Wang, Swing vibration control of suspended structures using the Active Rotary Inertia Driver system: theoretical modeling and experimental verification, *Struct. Contr. Health Monit.* 27 (6) (2020) 25–43, <https://doi.org/10.1002/stc.2543>.
- C. Li, L. Sun, Z. Xu, X. Wu, T. Liang, W. Shi, Experimental investigation and error analysis of high precision FBG displacement sensor for structural health monitoring, *Int. J. Struct. Stabil. Dynam.* 20 (2020) 2040011, <https://doi.org/10.1142/S0219455420400118>, 06.
- H. Li, D. Chen, H. Zhang, C. Wu, X. Wang, Hamiltonian analysis of a hydro-energy generation system in the transient of sudden load increasing, *Appl. Energy* 185 (2017) 244–253.
- B. Bai, Z. Guo, C. Zhou, W. Zhang, J. Zhang, Application of adaptive reliability importance sampling-based extended domain PSO on single mode failure in reliability engineering, *Inf. Sci.* 546 (2021) 42–59, <https://doi.org/10.1016/j.ins.2020.07.069>.
- L. Sun, C. Li, C. Zhang, Z. Su, C. Chen, Early monitoring of rebar corrosion evolution based on FBG sensor, *Int. J. Struct. Stabil. Dynam.* 18 (2018) 1840001, <https://doi.org/10.1142/S0219455418400011>, 08.

- [12] C. Zhang, Z. Alam, L. Sun, Z. Su, B. Samali, Fibre Bragg grating sensor-based damage response monitoring of an asymmetric reinforced concrete shear wall structure subjected to progressive seismic loads, *Struct. Contr. Health Monit.* 26 (3) (2019), e2307, <https://doi.org/10.1002/stc.2307>.
- [13] L. Sun, C. Li, C. Zhang, T. Liang, Z. Zhao, The strain transfer mechanism of fiber bragg grating sensor for extra large strain monitoring, *Sensors* 19 (8) (2019) 1851, <https://doi.org/10.3390/s19081851>.
- [14] C. HeapYih, L. CenYing, W. Xiangyu, A mixed review of the adoption of Building Information Modelling (BIM) for sustainability, *Journal of Cleaner Production* 142 (2017) 4114–4126, <https://doi.org/10.1016/j.jclepro.2016.09.222>.
- [15] Z. Dai, S. Guo, Y. Gong, Z. Wang, Semiconductor flexoelectricity in graphite-doped SrTiO<sub>3</sub> ceramics, *Ceram. Int.* 47 (5) (2021) 6535–6539, <https://doi.org/10.1016/j.ceramint.2020.10.239>.
- [16] C. Zhang, G. Gholipour, A.A. Mousavi, State-of-the-art review on responses of RC structures subjected to lateral impact loads, *Arch. Comput. Methods Eng.* (2020) 1–31, <https://doi.org/10.1007/s11831-020-09467-5>.
- [17] P. Wang, X. Zhang, W. Duan, W. Teng, Y. Liu, Q. Xie, Superhydrophobic flexible supercapacitors formed by integrating hydrogel with functional carbon nanomaterials, *Chin. J. Chem.* doi: <https://doi.org/10.1002/cjoc.202000543>.
- [18] H. Huang, M. Huang, W. Zhang, S. Pospisil, T. Wu, Experimental investigation on rehabilitation of corroded RC columns with bsp and hpfu under combined loadings, *J. Struct. Eng.* 146 (8) (2020), 04020157. <https://ascelibrary.org/doi/10.1061/28ASCE%29ST.1943-541X.0002725>.
- [19] Y. Ju, T. Shen, D. Wang, Bonding behavior between reactive powder concrete and normal strength concrete, *Construct. Build. Mater.* 242 (2020) 118024, <https://doi.org/10.1016/j.conbuildmat.2020.118024>.
- [20] M. Abedini, A.A. Mutalib, C. Zhang, J. Mehrmashhadi, S.N. Raman, R. Alipour, T. Momeni, M.H. Mussa, Large deflection behavior effect in reinforced concrete columns exposed to extreme dynamic loads, *Front. Struct. Civ. Eng.* 14 (2) (2020) 532–553, <https://doi.org/10.1007/s11709-020-0604-9>.
- [21] L. Jia, B. Liu, Y. Zhao, W. Chen, D. Mou, J. Fu, Y. Wang, W. Xin, L. Zhao, Structure design of MoS<sub>2</sub> @ Mo<sub>2</sub> C on nitrogen-doped carbon for enhanced alkaline hydrogen evolution reaction, *J. Mater. Sci.* 55 (34) (2020) 16197–16210, <https://doi.org/10.1007/s10853-020-05107-2>.
- [22] J. Zhang, M. Wang, Y. Tang, Q. Ding, C. Wang, X. Huang, D. Chen, F. Yan, Angular velocity measurement with improved scale factor based on a wideband-tunable optoelectronic oscillator, *IEEE Transactions on Instrumentation and Measurement* 70 (2021) 1–9, <https://doi.org/10.1109/TIM.2021.3067183>.
- [23] W. Jiao, A. Sha, Z. Liu, W. Jiang, L. Hu, X. Li, Utilization of steel slags to produce thermal conductive asphalt concretes for snow melting pavements, *J. Clean. Prod.* (2020) 121197.
- [24] J. Liu, Y. Yi, X. Wang, Exploring factors influencing construction waste reduction: a structural equation modeling approach, *J. Clean. Prod.* 276 (2020) 123–185, <https://doi.org/10.1016/j.jclepro.2020.123185>.
- [25] M. Abedini, C. Zhang, J. Mehrmashhadi, E. Akhlaghi, Comparison of ALE, LBE and Pressure Time History Methods to Evaluate Extreme Loading Effects in RC Column, *Elsevier*, p 456–466, doi: <https://doi.org/10.1016/j.istruc.2020.08.084>, 2020, pp. 456–466 doi: <https://doi.org/10.1016/j.istruc.2020.08.084>.
- [26] C. Zhang, A.A. Mousavi, Blast Loads Induced Responses of RC Structural Members: State-Of-The-Art Review, *Composites Part B: Engineering*, 2020, p. 108066, <https://doi.org/10.1016/j.compositesb.2020.108066>.
- [27] M. Abedini, C. Zhang, Dynamic performance of concrete columns retrofitted with FRP using segment pressure technique, *Compos. Struct.* 260 (2021) 113473, <https://doi.org/10.1016/j.compstruct.2020.113473>.
- [28] L. Wang, Y. Huang, Y. Xie, Y. Du, A new regularization method for dynamic load identification, *Sci. Prog.* 103 (3) (2020), 0036850420931283, <https://doi.org/10.1177/0036850420931283>.
- [29] W.B. Chaabene, M. Flah, M.L. Nehdi, Machine learning prediction of mechanical properties of concrete: critical review, *Construct. Build. Mater.* 260 (2020) 119889.
- [30] M. DeRousseau, J. Kasprzyk, W. Srubar III, Computational design optimization of concrete mixtures: a review, *Cement Concr. Res.* 109 (2018) 42–53.
- [31] W. Ben Chaabene, M. Flah, M.L. Nehdi, Machine learning prediction of mechanical properties of concrete: critical review, *Construct. Build. Mater.* 260 (2020) 119889.
- [32] W. Lei, Y. Jinling, W. Changzhi, W. Xiangyu, Practical algorithm for stochastic optimal control problem about microbial fermentation in batch culture, *Optimization Letters* 13 (3) (2017) 527–541.
- [33] L. Hou, S. Wu, G.K. Zhang, Y. Tan, X. Wang, Literature review of digital twins applications in construction workforce safety, *Appl. Sci.* 11 (1) (2021) 339.
- [34] L. Sun, Z. Yang, Q. Jin, W. Yan, Effect of axial compression ratio on seismic behavior of GFRP reinforced concrete columns, *Int. J. Struct. Stabil. Dynam.* 20 (2020) 2040004, <https://doi.org/10.1142/S0219455420400040>, 06.
- [35] H. Sun, C. Gao, Z. Zhang, X. Liao, X. Wang, J. Yang, High-resolution anisotropic prestress Kirchhoff dynamic focused beam migration, *IEEE Sensor. J.* 20 (20) (2019) 11753–11760, <https://doi.org/10.1109/JSEN.2019.2933200>.
- [36] C.J.B. Standard, China, GB/T, 50081-2002 Method for Testing Mechanical Properties of Normal Concrete, 2002.
- [37] W. Peng, W. Jun, W. Xiangyu, A critical review of the use of 3-D printing in the construction industry, *Automation in Construction* 68 (2016) 21–31.
- [38] L.J.M.I. Breiman, Random forests 45 (1) (2001) 5–32.
- [39] D.W. Hosmer Jr, S. Lemeshow, R.X. Sturdivant, Applied Logistic Regression, John Wiley & Sons 2013.
- [40] L.L. Nathans, F.L. Oswald, K. Nimon, Interpreting multiple linear regression: a guidebook of variable importance, *Practical Assess. Res. Eval.* 17 (9) (2012) 1–19.
- [41] J. Wang, H.J.a.p.a. Chen, BSAS: Beetle Swarm Antennae Search Algorithm for Optimization Problems, 2018.
- [42] L. Auret, C.J.M.E. Aldrich, Interpretation of Nonlinear Relationships between Process Variables by Use of Random Forests, vol. 35, 2012, pp. 27–42.
- [43] A. Kaveh, Applications of Metaheuristic Optimization Algorithms in Civil Engineering, Springer, 2017.
- [44] S. Vishal, G. Ning, W. Xiangyu, et al., A theoretical framework of a BIM-based multi-disciplinary collaboration platform 2nd, 20, *Automation in Construction*, 2011, pp. 134–144, <https://doi.org/10.1016/j.autcon.2010.09.011>.
- [45] R. Kohavi, A Study of Cross-Validation and Bootstrap for Accuracy Estimation and Model Selection, 1995, pp. 1137–1145. Ijcai, Montreal, Canada.
- [46] G. Gholipour, C. Zhang, A.A. Mousavi, Nonlinear numerical analysis and progressive damage assessment of a cable-stayed bridge pier subjected to ship collision, *Mar. Struct.* 69 (2020) 102662, <https://doi.org/10.1016/j.marstruc.2019.102662>.
- [47] C. Zhang, H. Wang, Robustness of the active rotary inertia driver system for structural swing vibration control subjected to multi-type hazard excitations, *Appl. Sci.* 9 (20) (2019) 4391, <https://doi.org/10.3390/app9204391>.
- [48] C. Zhang, G. Gholipour, A.A. Mousavi, Nonlinear dynamic behavior of simply-supported RC beams subjected to combined impact-blast loading, *Eng. Struct.* 181 (2019) 124–142, <https://doi.org/10.1016/j.engstruct.2018.12.014>.
- [49] Z. Alam, C. Zhang, B. Samali, The role of viscoelastic damping on retrofitting seismic performance of asymmetric reinforced concrete structures, *Earthq. Eng. Eng. Vib.* 19 (1) (2020) 223–237, <https://doi.org/10.1007/s11803-020-0558-x>.
- [50] Z. Alam, C. Zhang, B. Samali, Influence of seismic incident angle on response uncertainty and structural performance of tall asymmetric structure, *Struct. Des. Tall Special Build.* 29 (12) (2020), e1750, <https://doi.org/10.1002/tal.1750>.
- [51] H. Huang, M. Guo, W. Zhang, J. Zeng, K. Yang, H. Bai, Numerical investigation on the bearing capacity of RC columns strengthened by HPFL-BSP under combined loadings, *Journal of Building Engineering* (2021) 102266, <https://doi.org/10.1016/j.jobe.2021.102266>.
- [52] H. Huang, M. Huang, W. Zhang, S. Yang, Experimental study of predamaged columns strengthened by HPFL and BSP under combined load cases, *Structure and Infrastructure Engineering* (2020) 1–18, <https://doi.org/10.1080/15732479.2020.1801768>.
- [53] B. Mou, X. Li, Y. Bai, L. Wang, Shear behavior of panel zones in steel beam-to-column connections with unequal depth of outer annular stiffener, *J. Struct. Eng.* 145 (2) (2019), 04018247, [https://doi.org/10.1061/\(ASCE\)ST.1943-541X.0002256](https://doi.org/10.1061/(ASCE)ST.1943-541X.0002256).
- [54] L. Jing, Y. Pan, T. Wang, R. Qu, P.-T. Cheng, Transient analysis and verification of a magnetic gear integrated permanent magnet brushless machine with halbach arrays, *IEEE Journal of Emerging and Selected Topics in Power Electronics* (2021), <https://doi.org/10.1109/JESTPE.2021.3057665>.
- [55] J. Zheng, C. Zhang, A. Li, Experimental investigation on the mechanical properties of curved metallic plate dampers, *Appl. Sci.* 10 (1) (2020) 269, <https://doi.org/10.3390/app10010269>.
- [56] G. Gholipour, C. Zhang, A.A. Mousavi, Numerical analysis of axially loaded RC columns subjected to the combination of impact and blast loads, *Eng. Struct.* 219 (2020) 110924, <https://doi.org/10.1016/j.engstruct.2020.110924>.
- [57] C. Zhang, M. Abedini, J. Mehrmashhadi, Development of pressure-impulse models and residual capacity assessment of RC columns using high fidelity Arbitrary Lagrangian-Eulerian simulation, *Eng. Struct.* 224 (2020) 111219, <https://doi.org/10.1016/j.engstruct.2020.111219>.
- [58] X. Zuo, M. Dong, F. Gao, S. Tian, The modeling of the electric heating and cooling system of the integrated energy system in the coastal area, *J. Coast Res.* 103 (SI) (2020) 1022–1029, <https://doi.org/10.2112/SI103-213.1>.
- [59] N. Gao, J. Wu, K. Lu, H. Zhong, Hybrid composite meta-porous structure for improving and broadening sound absorption, *Mech. Syst. Signal Process.* 154 (2021) 107504, <https://doi.org/10.1016/j.ymssp.2020.107504>.
- [60] L. Zhu, L. Kong, C. Zhang, Numerical study on hysteretic behaviour of horizontal-connection and energy-dissipation structures developed for prefabricated shear walls, *Appl. Sci.* 10 (4) (2020) 1240, <https://doi.org/10.3390/app10041240>.
- [61] Z. Alam, L. Sun, C. Zhang, Z. Su, B. Samali, Experimental and numerical investigation on the complex behaviour of the localised seismic response in a multi-storey plan-asymmetric structure, *Structure and Infrastructure Engineering* 17 (1) (2021) 86–102, <https://doi.org/10.1080/15732479.2020.1730914>.
- [62] M. Abedini, C. Zhang, Performance assessment of concrete and steel material models in ls-dyna for enhanced numerical simulation, a state of the art review, *Arch. Comput. Methods Eng.* (2020) 1–22, <https://doi.org/10.1007/s11831-020-09483-5>.
- [63] R. Zhao, L. Zhang, G. Fan, Y. Chen, G. Huang, H. Zhang, J. Zhu, X. Guan, Probing the exact form and doping preference of magnesium in ordinary Portland cement clinker phases: a study from experiments and DFT simulations, *Cement Concr. Res.* 144 (2021) 106420, <https://doi.org/10.1016/j.cemconres.2021.106420>.
- [64] J. Zhu, K. Yang, Y. Chen, G. Fan, L. Zhang, B. Guo, X. Guan, R. Zhao, Revealing the substitution preference of zinc in ordinary Portland cement clinker phases: a study from experiments and DFT calculations, *J. Hazard Mater.* (2020) 124504, <https://doi.org/10.1016/j.jhazmat.2020.124504>.
- [65] J. Zhu, Y. Chen, L. Zhang, B. Guo, G. Fan, X. Guan, R. Zhao, Revealing the doping mechanism of barium in sulfoaluminate cement clinker phases, *J. Clean. Prod.* (2021) 126405, <https://doi.org/10.1016/j.jclepro.2021.126405>.
- [66] L. Cao, Changing port governance model: port spatial structure and trade efficiency, *J. Coast Res.* 95 (SI) (2020) 963–968, <https://doi.org/10.2112/SI95-187.1>.

- [67] M. Ye, J. Jiang, H. Chen, H. Zhou, D. Song, Seismic behavior of an innovative hybrid beam-column connection for precast concrete structures, Eng. Struct. 227 (2021) 111436, <https://doi.org/10.1016/j.engstruct.2021.111436>.
- [68] D. Yan, W. Wang, Q. Chen, Fractional-order modeling and nonlinear dynamic analyses of the rotor-bearing-seal system, Chaos, Solitons & Fractals 133 (2020) 109640, <https://doi.org/10.1016/j.chaos.2020.109640>.
- [69] C. Yang, F. Gao, M. Dong, Energy efficiency modeling of integrated energy system in coastal areas, J. Coast Res. 103 (SI) (2020) 995–1001, <https://doi.org/10.2112/SI103-207.1>.